

Quantitative relations among causality measures with applications to nonlinear pulse-output network reconstruction

Zhong-qi K. Tian^{a,b,c}, Kai Chen^{a,b,c}, Songting Li^{a,b,c,1}, David W. McLaughlin^{d,e,f,g,h,1}, and Douglas Zhou^{a,b,c,1}

^aSchool of Mathematical Sciences, Shanghai Jiao Tong University, Shanghai 200240, China

^bInstitute of Natural Sciences, Shanghai Jiao Tong University, Shanghai 200240, China

^cMinistry of Education Key Laboratory of Scientific and Engineering Computing, Shanghai Jiao Tong University, Shanghai 200240, China

^dCourant Institute of Mathematical Sciences, New York University, New York, NY 10012

^eCenter for Neural Science, New York University, New York, NY 10012

^fInstitute of Mathematical Sciences, New York University Shanghai, Shanghai 200122, China

^gNew York University Tandon School of Engineering, New York University, Brooklyn, NY 11201

^hNeuroscience Institute of New York University Langone Health, New York University, New York, NY 10016

Abstract. The causal connectivity of a network is often inferred to understand the network function. It is arguably acknowledged that the inferred causal connectivity relies on causality measure one applies, and it may differ from the network's underlying structural connectivity. However, the interpretation of causal connectivity remains to be fully clarified, in particular, how causal connectivity depends on causality measures and how causal connectivity relates to structural connectivity. Here, we focus on nonlinear networks with pulse signals as measured output, *e.g.*, neural networks with spike output, and address the above issues based on four intensively utilized causality measures, *i.e.*, time-delayed correlation, time-delayed mutual information, Granger causality, and transfer entropy. We theoretically show how these causality measures are related to one another when applied to pulse signals. Taking the simulated Hodgkin-Huxley neural network and the real mouse brain network as two illustrative examples, we further verify the quantitative relations among the four causality measures and demonstrate that the causal connectivity inferred by any of the four well coincides with the underlying network structural connectivity, therefore establishing a direct link between the causal and structural connectivity. We stress that the structural connectivity of networks can be reconstructed pairwise without conditioning on the global information of all other nodes in a network, thus circumventing the curse of dimensionality. Our framework provides a practical and effective approach for pulse-output network reconstruction.

Key words. causality, correlation, mutual information, Granger causality, transfer entropy, neural networks

Introduction

The structural connectivity of a network is of great importance to understand the cooperation and competition among nodes in the network. [1] However, it is often difficult to directly measure the structural connectivity of a network, for instance, the brain network. On the other hand, with the development of experimental techniques, it becomes feasible to record high-temporal-resolution activities of nodes in a network simultaneously [2-4]. This provides a possibility to reveal the underlying structural connectivity by analyzing the nodes' activity data and identifying the causal interactions (connectivity) among nodes [5-7]. One

of the most widely used statistical indicator for interaction identification is the correlation coefficient [8–10] that characterizes linear dependence between two nodes. Correlation coefficient is symmetric thus cannot distinguish the driver-recipient relation to recover the causal connectivity. To solve this, time-delayed correlation coefficient (TDCC) [10, 11] was introduced being able to detect the direction of causal connectivity. However, TDCC, as a linear measure, may fail to capture causal interactions in nonlinear networks. As a nonlinear generalization of TDCC, time-delayed mutual information (TDMI) [12–14] as a model-free measure was proposed to measure the flow of information in nonlinear networks. Despite the mathematical simplicity and computational efficiency of TDCC and TDMI, as pointed out in previous works, both measures cannot exclude the historical effect of signals and may encounter the issue of overestimation [13–15]. Granger causality (GC) [16–18] and transfer entropy (TE) [13, 19, 20] were another two measures to detect the causal connectivity with the exclusion of the historical effect of signal’s own. GC is based on linear regression models that assumes the causal relation can be revealed by analyzing low-order statistics (up to the variance) of signals. Consequently, the validity of GC for nonlinear networks is in general questionable [21]. In contrast, TE is a nonparametric information-theoretic measure that quantifies the causal interactions with no assumption of interaction models. However, it requires the estimation of the probability distribution of dynamical variables conditioning on the historical information in networks, which makes TE suffer from the curse of dimensionality in practical applications to network systems with many nodes [22–24].

Despite the broad application of the above causality measures, to interpret the results, two major theoretical issues remain to be clarified. First, what are the mathematical relations among these causality measures, *i.e.*, TDCC, TDMI, GC, and TE? It has been reported that the causal connectivity inferred by different causality measures in general can be inconsistent with one another [25–27]. Therefore, it is vital to understand the relation between different causal connectivity from those measures given certain conditions. We note that TE has been proven to be equivalent to GC for Gaussian variables [28], yet the mathematical relation among the four measures remains to be elucidated for general variables. Second, what is the relation between the causal connectivity and the structural connectivity? Note that the causal connectivity inferred by these measures is statistical rather than structural [29–31], *i.e.*, the causal connectivity quantifies directed statistical correlation or dependence among network nodes, whereas the structural connectivity corresponds to physical connections among network nodes. Therefore, it remains unclear whether the structural connectivity can be reconstructed from the causal connectivity in general.

In this work, we address these questions by investigating a general class of nonlinear networks with pulse signals as measured output, which we term as pulse-output networks. We first reveal the relations among TDCC, TDMI, GC, and TE with rigorous mathematical proofs. By taking the simulated Hodgkin-Huxley (HH) neural network and the real mouse brain network as two illustrative examples, we then verify the mathematical relations among the four causality measures numerically. We further demonstrate that the underlying structural connectivity of these networks can be recovered from the causal connectivity inferred using any of the above four causality measures. We emphasize that the structural connectivity can be reconstructed pairwise without conditioning on the global information of all other nodes, and thus circumvents the curse of dimensionality. Therefore, the reconstruction method based on these four causality measures can be applied to the reconstruction of structural connectivity in large-scale pulse-output nonlinear systems or subsystems.

Results

Concepts of generalized pairwise TDCC, TDMI, GC, and TE

Consider a nonlinear network of N nodes with dynamics given by

$$\frac{d\mathbf{Z}}{dt} = \mathbf{F}(\mathbf{Z}, t), \quad (1)$$

where $\mathbf{Z} = (Z_1, Z_2, \dots, Z_N)$. We focus on the application of TDCC, TDMI, GC, and TE to each pair of nodes without conditioning on the rest of nodes in the network, accounting for the practical constraint that conditional causality measure in general requires the information of the whole network that is often difficult to observe. For the ease of illustration, we denote a pair of nodes as $X = Z_i$ and $Y = Z_j$, and their measured time series as $\{x_n\}$ and $\{y_n\}$, respectively.

TDCC [10, 11], as a function of time delay m , is defined by

$$C(X, Y; m) = \frac{\text{cov}(x_n, y_{n-m})}{\sigma_x \sigma_y},$$

where ‘‘cov’’ represents the covariance, σ_x and σ_y are the standard deviations of $\{x_n\}$ and $\{y_n\}$, respectively. A positive (negative) value of m indicates the calculation of causal value from Y to X (from X to Y), and nonzero $C(X, Y; m)$ indicates the existence of causal interaction between X and Y . Without loss of generality, we consider the case of positive m in the following discussions, that is, the causality measure from Y to X .

In contrast to the linear measure TDCC, TDMI is a model-free method being able to characterize nonlinear causal interactions [12–14]. TDMI from Y to X is defined by

$$I(X, Y; m) = \sum_{x_n, y_{n-m}} p(x_n, y_{n-m}) \log \frac{p(x_n, y_{n-m})}{p(x_n)p(y_{n-m})}, \quad (2)$$

where $p(x_n, y_{n-m})$ is the joint probability distribution of x_n and y_{n-m} , $p(x_n)$ and $p(y_{n-m})$ are the corresponding marginal probability distributions. $I(X, Y; m)$ is non-negative and vanishes if and only if x_n and y_{n-m} are independent [14]. Nonzero $I(X, Y; m)$ implies the existence of causal interaction from Y to X for a positive m .

It has been noted that TDCC and TDMI could overestimate the causal interactions when a signal has a long memory [13–15]. As an alternative, GC was proposed to overcome the issue of overestimation based on linear regression [16, 17, 32]. The auto-regression for X is represented by $x_{n+1} = a_0 + \sum_{i=1}^k a_i x_{n+1-i} + \epsilon_{n+1}$, where $\{a_i\}$ are the auto-regression coefficients and ϵ_{n+1} is the residual. By including the historical information of Y with a message length l and a time-delay m , the joint regression for X is represented by $x_{n+1} = \tilde{a}_0 + \sum_{i=1}^k \tilde{a}_i x_{n+1-i} + \sum_{j=1}^l b_j y_{n+2-m-j} + \eta_{n+1}$, where $\{\tilde{a}_i\}$ and $\{b_j\}$ are the joint regression coefficients, and η_{n+1} is the corresponding residual. If there exists a causal interaction from Y to X , then the prediction of X using the linear regression models shall be improved by additionally incorporating the historical information of Y . Accordingly, the variance of residual η_{n+1} is smaller than that of ϵ_{n+1} . Based on this concept, the GC value from Y to X is defined by

$$G_{Y \rightarrow X}(k, l; m) = \log \frac{\text{Var}(\epsilon_{n+1})}{\text{Var}(\eta_{n+1})}.$$

The GC value is also non-negative and vanishes if and only if $\{b_j\} = 0$, *i.e.*, the variance of residual ϵ_{n+1} for X cannot be reduced by including the historical information of Y . Note that, by introducing the time-delay parameter m , the GC analysis defined above generalizes the conventional GC analysis, as the latter corresponds to the special case of $m = 1$.

GC assumes that the causal interaction can be fully captured by the variance reduction in the linear regression models, which is valid for Gaussian signals but not for more general signals. As a nonlinear extension of GC, TE was proposed to describe the causal interaction from the information theoretic perspective [13]. The TE value from Y to X is defined by

$$T_{Y \rightarrow X}(k, l; m) = \sum_{x_{n+1}, x_n^{(k)}, y_{n+1-m}^{(l)}} p(x_{n+1}, x_n^{(k)}, y_{n+1-m}^{(l)}) \cdot \log \frac{p(x_{n+1} | x_n^{(k)}, y_{n+1-m}^{(l)})}{p(x_{n+1} | x_n^{(k)})}, \quad (3)$$

where the shorthand notation $x_n^{(k)} = (x_n, x_{n-1}, \dots, x_{n-k+1})$ and $y_{n+1-m}^{(l)} = (y_{n+1-m}, y_{n-m}, \dots, y_{n+2-m-l})$, k, l indicate the length (order) of historical information of X and Y , respectively. Similar to GC, the time-delay parameter m is introduced that generalizes the conventional TE, the latter of which corresponds to the case of $m = 1$. TE is non-negative and vanishes if and only if $p(x_{n+1}|x_n^{(k)}, y_{n+1-m}^{(l)}) = p(x_{n+1}|x_n^{(k)})$, *i.e.*, the uncertainty of x_{n+1} is not affected regardless of whether the historical information of Y is taken into account.

In this work, we investigate the mathematical relations among TDCC, TDMI, GC, and TE by focusing on nonlinear networks described by Eq. 1 with pulse signals as measured output, *e.g.*, the spike trains measured in neural networks. Consider a pair of nodes X and Y in the network of N nodes, and denote their pulse-output signals by

$$w_x(t) = \sum_l \delta(t - \tau_{xl}) \quad \text{and} \quad w_y(t) = \sum_l \delta(t - \tau_{yl}), \quad (4)$$

respectively, where $\delta(\cdot)$ is the Dirac delta function, and $\{\tau_{xl}\}$ and $\{\tau_{yl}\}$ are the output time sequences of nodes X and Y determined by Eq. 1, respectively. With the sampling resolution of Δt , the pulse-output signals are measured as binary time series $\{x_n\}$ and $\{y_n\}$, where $x_n = 1$ ($y_n = 1$) if there is a pulse signal, *e.g.*, a spike generated by a neuron, of X (Y) occurred in the time window $[t_n, t_n + \Delta t)$, and $x_n = 0$ ($y_n = 0$) otherwise, *i.e.*,

$$x_n = \int_{t_n}^{t_n + \Delta t} w_x(t) dt \quad \text{and} \quad y_n = \int_{t_n}^{t_n + \Delta t} w_y(t) dt, \quad (5)$$

and $t_n = n\Delta t$. Note that the value of Δt is often chosen to make sure that there is at most one pulse signal in a single time window. In the stationary resting state, the responses x_n and y_n can be viewed as stochastic processes when the network is driven by stochastic external inputs. In such a case, for the sake of simplicity, we denote $p_x = p(x_n = 1)$, $p_y = p(y_n = 1)$, and $\Delta p_m = \frac{p(x_n=1, y_{n-m}=1)}{p(x_n=1)p(y_{n-m}=1)} - 1$ that measures the dependence between x_n and y_{n-m} .

Mathematical relation between TDMI and TDCC

For the relation between TDCC and TDMI when applied to the above nonlinear networks with pulse-output signals, we prove the following theorem:

Theorem 1. *For nodes X and Y with pulse-output signals given in Eqs. 4 and 5, we have*

$$I(X, Y; m) = \frac{C^2(X, Y; m)}{2} + O(\Delta t^2 \Delta p_m^3), \quad (6)$$

where the symbol “ O ” stands for the order.

Proof. The basic idea is to Taylor expand TDMI in Eq. 2 with respect to the term $\frac{p(x_n, y_{n-m})}{p(x_n)p(y_{n-m})} - 1$ (the detailed derivation can be found in *SI Appendix, Supplementary Information Text 1B*), then we arrive at the following expression:

$$\begin{aligned} I(X, Y; m) &= \sum_{x_n, y_{n-m}} p(x_n, y_{n-m}) \log \left(1 + \frac{p(x_n, y_{n-m})}{p(x_n)p(y_{n-m})} - 1 \right) \\ &= \frac{[p(x_n = 1, y_{n-m} = 1) - p_x p_y]^2}{2(p_x - p_x^2)(p_y - p_y^2)} + O(\Delta t^2 \Delta p_m^3). \end{aligned}$$

By definition,

$$C(X, Y; m) = \frac{p(x_n = 1, y_{n-m} = 1) - p_x p_y}{\sqrt{(p_x - p_x^2)(p_y - p_y^2)}}, \quad (7)$$

we have

$$I(X, Y; m) = \frac{C^2(X, Y; m)}{2} + O(\Delta t^2 \Delta p_m^3).$$

□

Mathematical relation between GC and TDCC

We next derive the relation between GC and TDCC as follows:

Theorem 2. For nodes X and Y with pulse-output signals given in Eqs. 4 and 5, we have

$$G_{Y \rightarrow X}(k, l; m) = \sum_{i=m}^{m+l-1} C^2(X, Y; i) + O(\Delta t^3 \Delta p_m^2). \quad (8)$$

Proof. From the definition, GC can be represented by the covariances of the signals [28] as

$$G_{Y \rightarrow X}(k, l; m) = \log \frac{\Gamma(x_{n+1}|x_n^{(k)})}{\Gamma(x_{n+1}|x_n^{(k)} \oplus y_{n+1-m}^{(l)})}, \quad (9)$$

where $\Gamma(\mathbf{x}|\mathbf{y}) = \text{cov}(\mathbf{x}) - \text{cov}(\mathbf{x}, \mathbf{y})\text{cov}(\mathbf{y})^{-1}\text{cov}(\mathbf{x}, \mathbf{y})^T$ for random vectors \mathbf{x} and \mathbf{y} , $\text{cov}(\mathbf{x})$ and $\text{cov}(\mathbf{y})$ denote the covariance matrix of \mathbf{x} and \mathbf{y} , respectively, and $\text{cov}(\mathbf{x}, \mathbf{y})$ denote the cross-covariance matrix between \mathbf{x} and \mathbf{y} . The symbol T is the transpose operator and \oplus denotes the concatenation of vectors.

We first prove that the auto-correlation function (ACF) of binary time series $\{x_n\}$ as a function of time delay takes the order of Δt (see [SI Appendix, Supplementary Information Text 1C](#) for the proof, [Fig. S1](#)). Accordingly, we have

$$\text{cov}(x_n^{(k)}) = \sigma_x^2(\mathbf{I} + \hat{\mathbf{A}}),$$

where $\hat{\mathbf{A}} = (\hat{a}_{ij})$, $\hat{a}_{ij} = O(\Delta t)$, and \mathbf{I} is the identity matrix. Hence,

$$\begin{aligned} \Gamma(x_{n+1}|x_n^{(k)}) &= \sigma_x^2 - \frac{1}{\sigma_x^2} \text{cov}(x_{n+1}, x_n^{(k)})(\mathbf{I} - \hat{\mathbf{A}}) \\ &\quad \cdot \text{cov}(x_{n+1}, x_n^{(k)})^T + O(\Delta t^5). \end{aligned} \quad (10)$$

In the same way, we have

$$\begin{aligned} &\Gamma(x_{n+1}|x_n^{(k)} \oplus y_{n+1-m}^{(l)}) \\ &= \sigma_x^2 - \frac{1}{\sigma_x^2} \text{cov}(x_{n+1}, x_n^{(k)})(\mathbf{I} - \hat{\mathbf{A}}) \text{cov}(x_{n+1}, x_n^{(k)})^T \\ &\quad - \frac{1}{\sigma_y^2} \text{cov}(x_{n+1}, y_{n+1-m}^{(l)})(\mathbf{I} - \hat{\mathbf{B}}) \text{cov}(x_{n+1}, y_{n+1-m}^{(l)})^T \\ &\quad + O(\Delta t^4 \Delta p_m^2). \end{aligned} \quad (11)$$

where $\hat{\mathbf{B}} = (\hat{b}_{ij})$, $\hat{b}_{ij} = O(\Delta t)$. Substituting Eqs. 10 and 11 into Eq. 9 and Taylor expanding Eq. 9 with respect to Δt , we can obtain

$$G_{Y \rightarrow X}(k, l; m) = \sum_{i=m}^{m+l-1} C^2(X, Y; i) + O(\Delta t^3 \Delta p_m^2). \quad (12)$$

The detailed derivation of Eqs. 10, 11, and 12 can be found in [SI Appendix, Supplementary Information Text 1C](#). □

Mathematical relation between TE and TDMI

From the generalized definitions of TE and TDMI, TE can be regarded as a generalization of TDMI conditioning on the signals' historical information additionally. To rigorously establish their relationship, we require that $\|x_{n+1}^{(k+1)}\|_0 \leq 1$ and $\|y_{n+1-m}^{(l)}\|_0 \leq 1$ in the definition of TE given in Eq. 3, where $\|\cdot\|_0$ denotes the l_0 norm of a vector, *i.e.*, the number of nonzero elements in a vector. This assumption indicates that the length of historical information used in the TE framework is shorter than the minimal time interval between two consecutive pulse-output signals. This condition is often satisfied for nonlinear network with output signals. Consequently, we have the following theorem:

Theorem 3. For nodes X and Y with pulse-output signals given in Eqs. 4 and 5, we have

$$T_{Y \rightarrow X}(k, l; m) = \sum_{i=m}^{m+l-1} I(X, Y; i) + O(\Delta t^3 \Delta p_m^2), \quad (13)$$

where $T_{Y \rightarrow X}$ is defined in Eq. 3 with the assumption that $\|x_{n+1}^{(k+1)}\|_0 \leq 1$ and $\|y_{n+1-m}^{(l)}\|_0 \leq 1$.

Proof. To simplify the notations, we denote $x_n^{(k)} = (x_n, x_{n-1}, \dots, x_{n-k+1})$ and $y_{n+1-m}^{(l)} = (y_{n+1-m}, y_{n-m}, \dots, y_{n+2-m})$ as x^- and y^- , respectively. From Eq. 3, we have

$$\begin{aligned} T_{Y \rightarrow X}(k, l; m) &= \sum_{x_{n+1}, x^-, y^-} p(x_{n+1}, x^-, y^-) \log \frac{p(x_{n+1} | x^-, y^-)}{p(x_{n+1} | x^-)} \\ &= \sum_{i=m}^{m+l-1} I(X, Y; i) + \mathcal{A} + \mathcal{B}, \end{aligned} \quad (14)$$

where

$$\mathcal{A} = \sum_{x_{n+1}, y^-} p(x_{n+1}, y^-) \log \frac{p(y^- | x_{n+1})}{\prod_j p(y_j | x_{n+1})} \frac{\prod_j p(y_j)}{p(y^-)}$$

and

$$\mathcal{B} = \sum_{x_{n+1}, x^-, y^-} p(x_{n+1}, x^-, y^-) \log \frac{p(x_{n+1} | x^-, y^-)}{p(x_{n+1} | y^-)} \frac{p(x_{n+1})}{p(x_{n+1} | x^-)}$$

and \prod_j in \mathcal{A} represents $\prod_{j=n+2-m-l}^{n+1-m}$. The detailed derivation of Eq. 14 can be found in [SI Appendix, Supplementary Information Text 1D](#). \mathcal{A} and \mathcal{B} in Eq. 14 consist of multiple terms and the leading order of each term can be analytically calculated. For the sake of illustration, below we derive the leading order of one of these terms and the leading order of the rest terms can be estimated in a similar way. Under the assumption that $\|x_{n+1}^{(k+1)}\|_0 \leq 1$ and $\|y_{n+1-m}^{(l)}\|_0 \leq 1$, the number of nonzero components is at most one in $x_{n+1}^{(k+1)}$ and $y_{n+1-m}^{(l)}$. Without loss of generality, we assumed $x_{n+1} = 1$ and $y_{n+1-m} = 1$. In such a case, we can obtain the following expression in \mathcal{A} ,

$$\begin{aligned} & p(x_{n+1}, y^-) \log \frac{p(y^- | x_{n+1})}{\prod_j p(y_j | x_{n+1})} \frac{\prod_j p(y_j)}{p(y^-)} \Big|_{x_{n+1}=1, y_{n+1-m}=1} \\ &= p_x p_y^2 \sum_{j \neq n+1-m} \Delta p_{n+1-j} + O(\Delta t^3 \Delta p_m^2). \end{aligned}$$

We can further show that the leading order of all the terms in \mathcal{A} happen to cancel each other out ([SI Appendix, Supplementary Information Text 1D](#)), thus we have $\mathcal{A} = O(\Delta t^3 \Delta p_m^2)$. Similarly, we can also show $\mathcal{B} = O(\Delta t^3 \Delta p_m^2)$ ([SI Appendix, Supplementary Information Text 1D](#)), and thus

$$T_{Y \rightarrow X}(k, l; m) = \sum_{i=m}^{m+l-1} I(X, Y; i) + O(\Delta t^3 \Delta p_m^2).$$

□

Mathematical relation between GC and TE

From Theorems 1-3, we can straightforwardly prove the following theorem:

Theorem 4. For nodes X and Y with pulse-output signals given in Eqs. 4 and 5, we have

$$G_{Y \rightarrow X}(k, l; m) = 2T_{Y \rightarrow X}(k, l; m) + O(\Delta t^2 \Delta p_m^3), \quad (15)$$

where $T_{Y \rightarrow X}$ is defined in Eq. 3 with the assumption that $\|x_{n+1}^{(k+1)}\|_0 \leq 1$ and $\|y_{n+1-m}^{(l)}\|_0 \leq 1$.

Note that in Theorems 3 and 4 we have the extra assumption $\|x_{n+1}^{(k+1)}\|_0 \leq 1$ and $\|y_{n+1-m}^{(l)}\|_0 \leq 1$. As numerically verified below, the extra assumption is often easily satisfied to achieve the successful application of these causality measures. For example, the memory time of the neuron is about 20 ms, while the inter-spike interval is around 100 ms. The extra assumption is to rigorously establish the relations in Theorems 3 and 4, but is not a necessary condition (SI Appendix, Fig. S2). We summarize the relations among the four causality measures in Fig. 1.

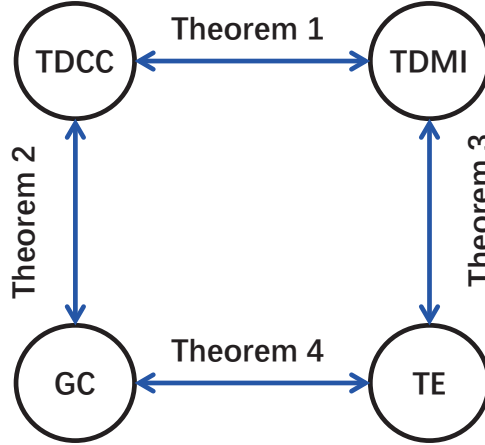


Figure 1: Mathematical relations among TDCC, TDMI, GC, and TE.

Mathematical relations of causality measures verified in HH neural networks

To verify the relations among the causality measures derived above, as an illustrative example, we apply generalized pairwise TDCC, TDMI, GC, and TE to the HH neural network described in *Materials and Methods*. We first consider a pair of neurons denoted by X and Y with unidirectional connection from Y to X in an HH network containing 10 excitatory neurons driven by homogeneous Poisson inputs. Let $\{\tau_{xl}\}$ and $\{\tau_{yl}\}$ be the ordered spike times of neuron X and Y in the HH network respectively and denote their spike trains as $w_x(t) = \sum_l \delta(t - \tau_{xl})$ and $w_y(t) = \sum_l \delta(t - \tau_{yl})$, respectively. With a sampling resolution of Δt , the spike train is measured as a binary time series as described above. To numerically verify the above theorems, we then check the order of the remainders in Eqs. 6, 8, 13, and 15 in terms of

Δt and Δp_m . Note that Δp_m , the measure of the dependence between X and Y , is insensitive to sampling resolution Δt (*SI Appendix, Fig. S3*). Therefore, by varying sampling interval Δt and coupling strength S (linearly related to Δp_m) respectively, the orders of the remainders are consistent with those derived in Eqs. 6, 8, 13, and 15 (Fig. 2). In addition, Fig. 3 verifies the relations among the causality measures by changing other parameters. For example, in Eqs. 8, 13, and 15, the four causality measures are proved to be independent of the historical length k , which is numerically verified in Fig. 3A. And although the values of GC and TE rely on the historical length l (Fig. 3B), the mathematical relations among the four causality measures revealed by Theorems 1-4 hold for a wide range of l . We next verify the mathematical relations among the causality measures for the parameter of time delay m by fixing parameters k and l . In principle, the value of k and l in GC and TE shall be determined by the historical memory of the system. To reduce the computational cost [10, 33, 34], we take $k = l = 1$ for all the results below. It turns out that this parameter choice works well for pulse-output networks because of the short memory effect in general, as will be further discussed later. Fig. 3C shows the mathematical relations hold for a wide range of time delay parameter used in computing the four causality measures.

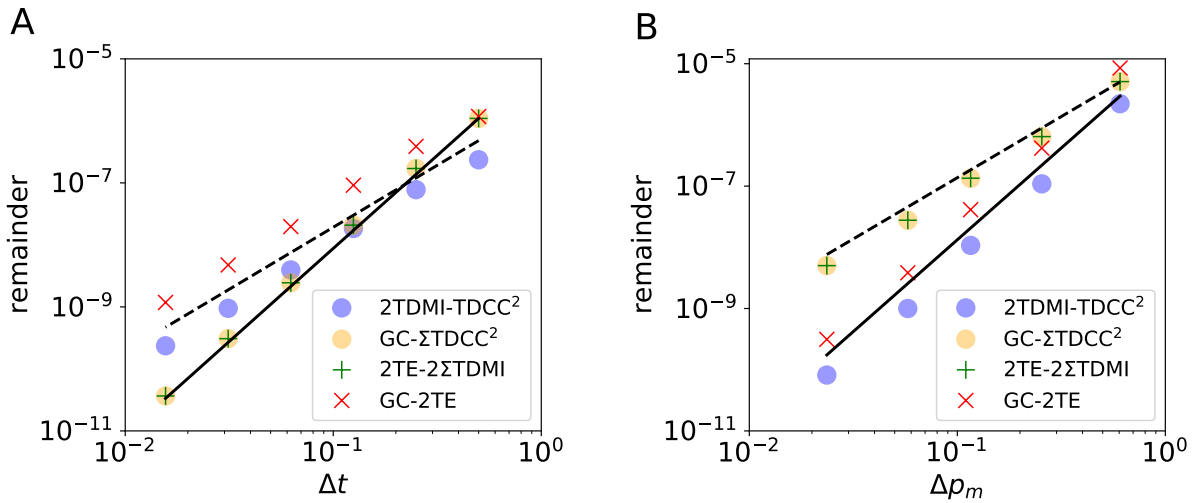


Figure 2: Convergence order of the remainders in terms of (A) Δt and (B) Δp_m obtained from causality measures from neuron Y to neuron X with unidirectional connection from Y to X in an HH network of 10 excitatory neurons randomly connected with probability 0.25. The convergence orders for Δt in (A) fit with which shows in Theorems 1-4 ($R^2 > 0.998$), while those for Δp_m in (B) fit the values derived in Theorems 1-4 ($R^2 > 0.998$). The gray dashed and solid lines indicate the 2nd-order and 3rd-order convergence, respectively. The parameters are set as $k = l = 5$ and $m = 6$ (time delay is 3 ms), $S = 0.02$ mS \cdot cm $^{-2}$ in (A), and $\Delta t = 0.5$ ms in (B).

We further examine the robustness of the mathematical relations among TDCC, TDMI, GC, and TE by scanning the parameters of the coupling strength S between the HH neurons and external Poisson input strength and rates. As shown in Fig. 3D, the values of the four causality measures with different coupling strength are very close to one another. Their relations also hold for a wide range of external Poisson input parameters (*SI Appendix, Fig. S4*). From the above, the mathematical relations among TDCC, TDMI, GC, and TE described in Theorems 1-4 are verified in the HH network.

Relation between structural connectivity and causal connectivity in HH neural networks

We next discuss about the relation between the inferred causal connectivity and the structural connectivity. Note that the causal connectivity inferred by these measures are statistical rather than structural [29–31], *i.e.*, the causal connectivity quantifies the directed statistical correlation or dependence among network

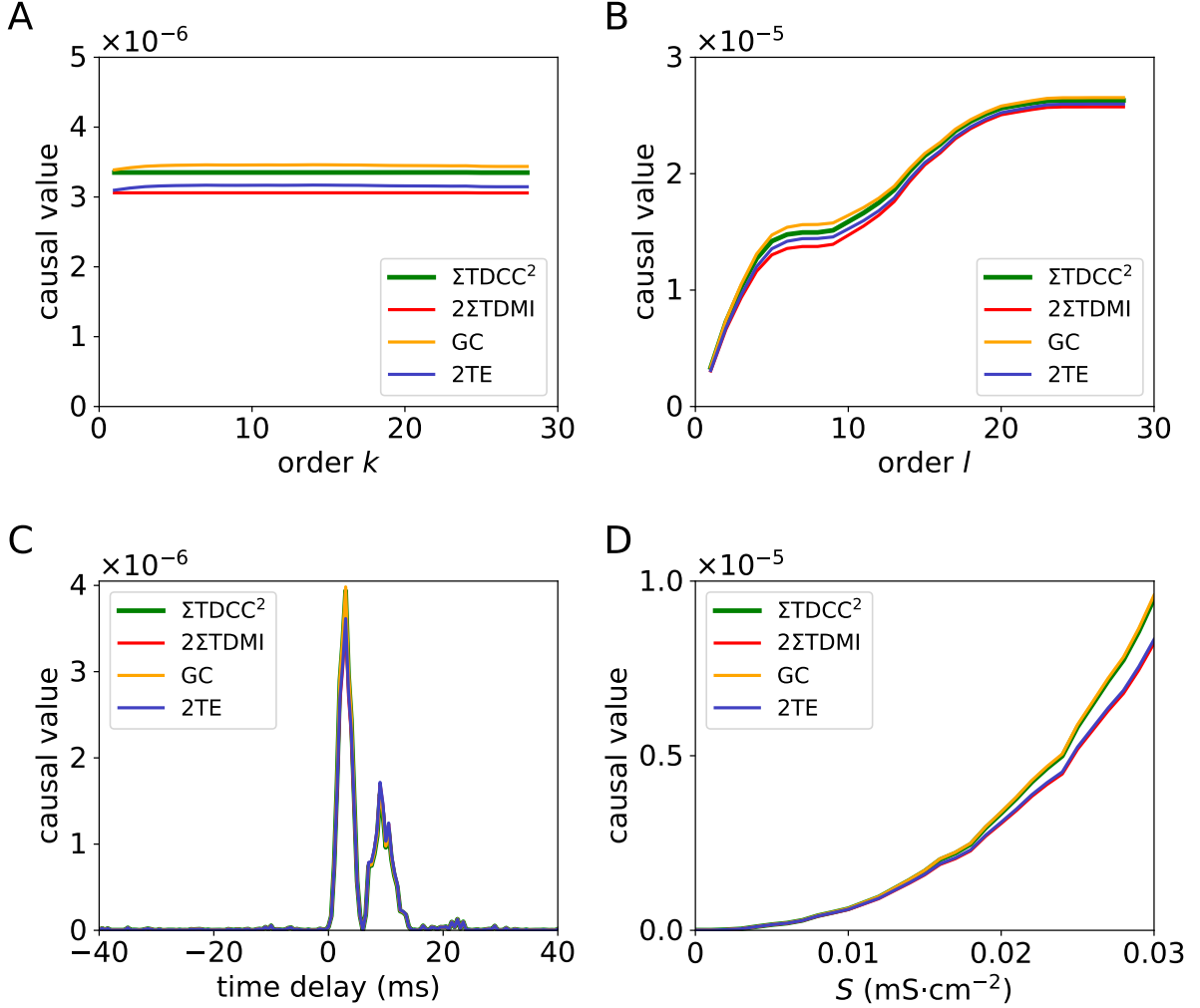


Figure 3: Dependence of causal values on parameters of (A) order k , (B) order l , (C) time delay, and (D) coupling strength S obtained from neuron Y to neuron X in the HH network in Fig. 2. In (C), a positive (negative) time delay indicates the calculation of causal values from Y to X (from X to Y). The curves of causal values reach the peak at the time delay 3 ms ($m = 6$) in (C). The green curve represents the summation of square of TDCC $C(X, Y; m)$, the red curve represents two times the summation of TDMI $I(X, Y; m)$, the orange curve stands for GC $G_{Y \rightarrow X}(k, l; m)$, and the blue curve stands for twice of TE $T_{Y \rightarrow X}(k, l; m)$. The curves are close to each other in (A)-(D) and virtually overlap (all significantly greater than those of randomly surrogate time series, $p < 0.05$). The parameters are set as (A): $l = 1$, $S = 0.02 \text{ mS}\cdot\text{cm}^{-2}$, $\Delta t = 0.5 \text{ ms}$, $m = 6$; (B): $k = 1$, $S = 0.02 \text{ mS}\cdot\text{cm}^{-2}$, $\Delta t = 0.5 \text{ ms}$, $m = 6$; (C): $k = l = 1$, $S = 0.02 \text{ mS}\cdot\text{cm}^{-2}$, $\Delta t = 0.5 \text{ ms}$; (D): $k = l = 1$, $\Delta t = 0.5 \text{ ms}$, $m = 6$.

nodes, whereas the structural connectivity corresponds to physical connections among network nodes. Therefore, it remains unclear about the relationship between the causal connectivity and the structural connectivity. In Fig. 3C, the peak causal value from Y to X (at time delay around 3 ms, $m=6$) is significantly greater than threshold, while the causal value from X to Y is not. Based on this, the inferred causal connections between X and Y are consistent with the underlying structural connections. From now on, we adopt peak causal values, $m=6$, to represent the causal connectivity unless noted explicitly. To investigate the validity of this consistency in larger networks, we further investigate a larger HH network (100 excitatory neurons) with random connectivity (*SI Appendix, Fig. S5A*). As shown in Fig. 4A, the distributions of all four causal values across all pairs of neurons virtually overlapped, which again verify their mathematical relations given by Theorems 1-4. In addition, as the network size increases, the distributions of the causality measures in Fig. 4A exhibits a bimodal structure with a clear separation of orders. By mapping the causal values with the structural connectivity, we find that the right bump of the distributions with larger causal values corresponded to connected pairs of neurons, while the left bump with smaller causal values corresponded to unconnected pairs. The well separation of the two modals indicates that the underlying structural connectivity in the HH network can be accurately reconstructed by the causal connectivity. The performance of this reconstruction approach can be quantitatively characterized by the receiver operating characteristic (ROC) curve and the area under the ROC curve (AUC) [25,35,36] (*Materials and Methods*). It is found that the AUC value became 1 when applying any of these four causality measures (*SI Appendix, Fig. S5B*), which indicates that the structural connectivity of the HH network could be reconstructed with 100 % accuracy. We point out that the reconstruction of network connectivity based on causality measures is achieved by calculating the causal values between each pair of neurons that required no access towards the activity data of the rest of neurons. Therefore, this inference approach can be applied to a subnetwork when the activity of neurons outside the subnetwork is not observable. For example, when a subnetwork of 20 excitatory HH neurons is observed, the structural connectivity of the subnetwork can still be accurately reconstructed without knowing the information of the rest 80 neurons in the full network (Fig. 4B). In such a case, the AUC values corresponding to the four causality measures are 1 (*SI Appendix, Fig. S5C*).

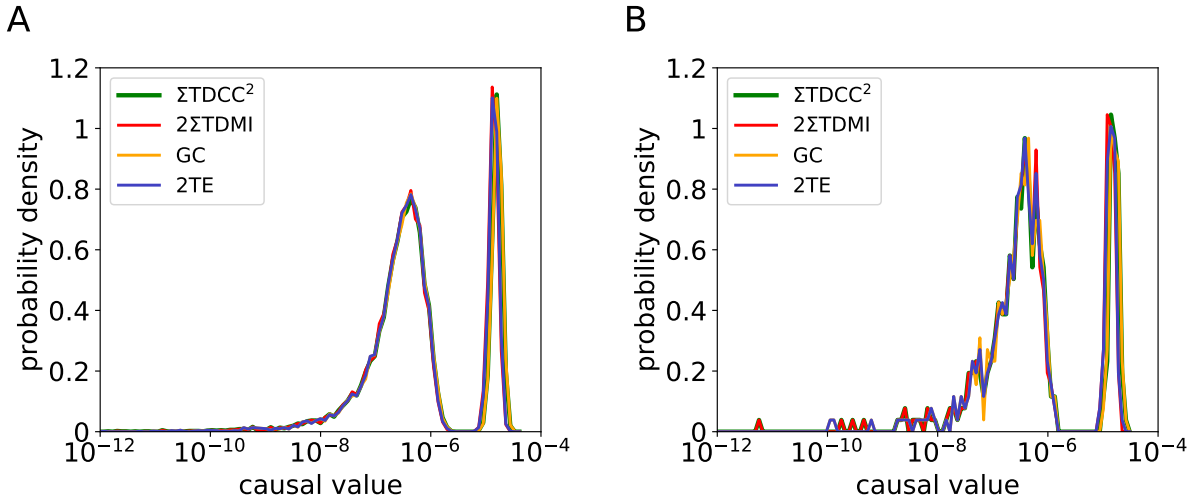


Figure 4: Distributions of causal values in an HH network of 100 excitatory neurons randomly connected with probability 0.25. (A) The distribution of causal values of each pair of neurons in the whole network. (B) The distribution of causal values of each pair of neurons in an HH subnetwork of 20 excitatory neurons. The parameters are set as $k = l = 1$, and $S = 0.02 \text{ mS}\cdot\text{cm}^{-2}$, $\Delta t = 0.5 \text{ ms}$, and $m = 6$ (3 ms). The colors are the same as those in Fig. 3 and the curves nearly overlap.

Mechanism underlying network connectivity reconstruction by causality measures

We next demonstrate the mechanism of pairwise inference on pulse-output signals in the reconstruction of network structural connectivity. It has been noticed that pairwise causal inference may potentially fail to distinguish the direct interactions from the indirect ones in a network. For example, in the case that $Y \rightarrow W \rightarrow X$ where “ \rightarrow ” denotes a directed connection, the indirect interaction from Y to X may possibly be mis-inferred as a direct interaction via pairwise causality measures. However, such spurious inference can be circumvented in our generalized pairwise causality measured based on pulse-output signals as explained below. Here we take TDCC as an example to elucidate the underlying reason of successful reconstruction. If we denote $\delta p_{Y \rightarrow X} = p(x_n = 1 | y_{n-m} = 1) - p(x_n = 1 | y_{n-m} = 0)$ as the increment of probability of generating a pulse output for neuron X induced by a pulse-output signal of neuron Y at m time step earlier, we have TDCC $C(X, Y; m) = \delta p_{Y \rightarrow X} \sqrt{\frac{p_y - p_y^2}{p_x - p_x^2}}$ through Eq. 7. For the case of $Y \rightarrow W \rightarrow X$, we can derive $\delta p_{Y \rightarrow X} = O(\delta p_{Y \rightarrow W} \cdot \delta p_{W \rightarrow X})$ (details in *SI Appendix, Supplementary Information Text 2*). Because the influence of a single pulse output signal is often small (e.g., in the HH neural network with physiologically realistic coupling strengths, we obtain $|\delta p| < 0.01$ from simulation data), the causal value $C(X, Y; m)$ due to the indirect interaction is significantly smaller than $C(W, Y; m)$ or $C(X, W; m)$ by direct interactions (Fig. 4A).

We also note that the increment δp is linearly dependent on the coupling strength S (*SI Appendix, Fig. S6*), thus we establish a mapping between the causal and structural connectivity, in which the causal value of TDCC is proportional to the coupling strength S between two neurons. The mapping between causal and structural connectivity for TDMI, GC, and TE are also established in a similar way, in which the corresponding causal values are proportional to S^2 . Therefore, the application of pairwise causality measures to pulse-output signals is able to successfully reveal the underlying structural connectivity of a network. Importantly, this approach overcame the computational issue of high dimensionality, thus is potentially applicable to data of large-scale networks or subnetworks measured in experiments.

Network connectivity reconstruction with physiological experimental data

Next, we apply all four causality measures to experimental data to address the issue of validity of their mathematical relations and reconstruction of the network structural connectivity. Here, we analyze the in vivo spike data recorded in the mouse brain from Allen Brain Observatory [37] (details in *Materials and Methods*). By applying the four causality measures, we infer the causal connectivity of those brain networks. As the underlying structural connectivity of the recorded neurons in experiments was unknown, we first detect putative connected links from the distribution of causality measures as introduced below, and then follow the same procedures as previously described in the HH model case using ROC and AUC in signal detection theory [25, 35, 36] (*Materials and Methods*) to quantify the reconstruction performance.

Since demonstrated the equivalence of four causality measures, we choose TE as an example for the discussion below. As we have proved above, the TE values are proportional to S^2 . Besides, previous experimental works observed that the structural connectivity S follows the log-normal distribution both for cortico-cortical and local networks in mouse and monkey brains [38]. Thus, the distribution of TE should also follow the log-normal distribution. Therefore, we fit the distribution of TE values for experimental data with the summation of two log-normal likelihood functions (details in *Materials and Methods*).

As an illustrative example, we consider an HH network where neurons receive correlated background Poisson input. In this case, although the distribution of TE values $\log_{10} T_{Y \rightarrow X}$ (Fig. 5A) for synaptically connected and unconnected pairs of neurons overlap with each other, it is still well fitted by the summation of two log-normal distributions of TE values. More importantly, the fitted distribution of TE from connected and unconnected pairs agreed well with those from the true connectivity used in simulation (Fig. 5B). Thus, we take the fitted causality measure distributions as the ground truth of structural

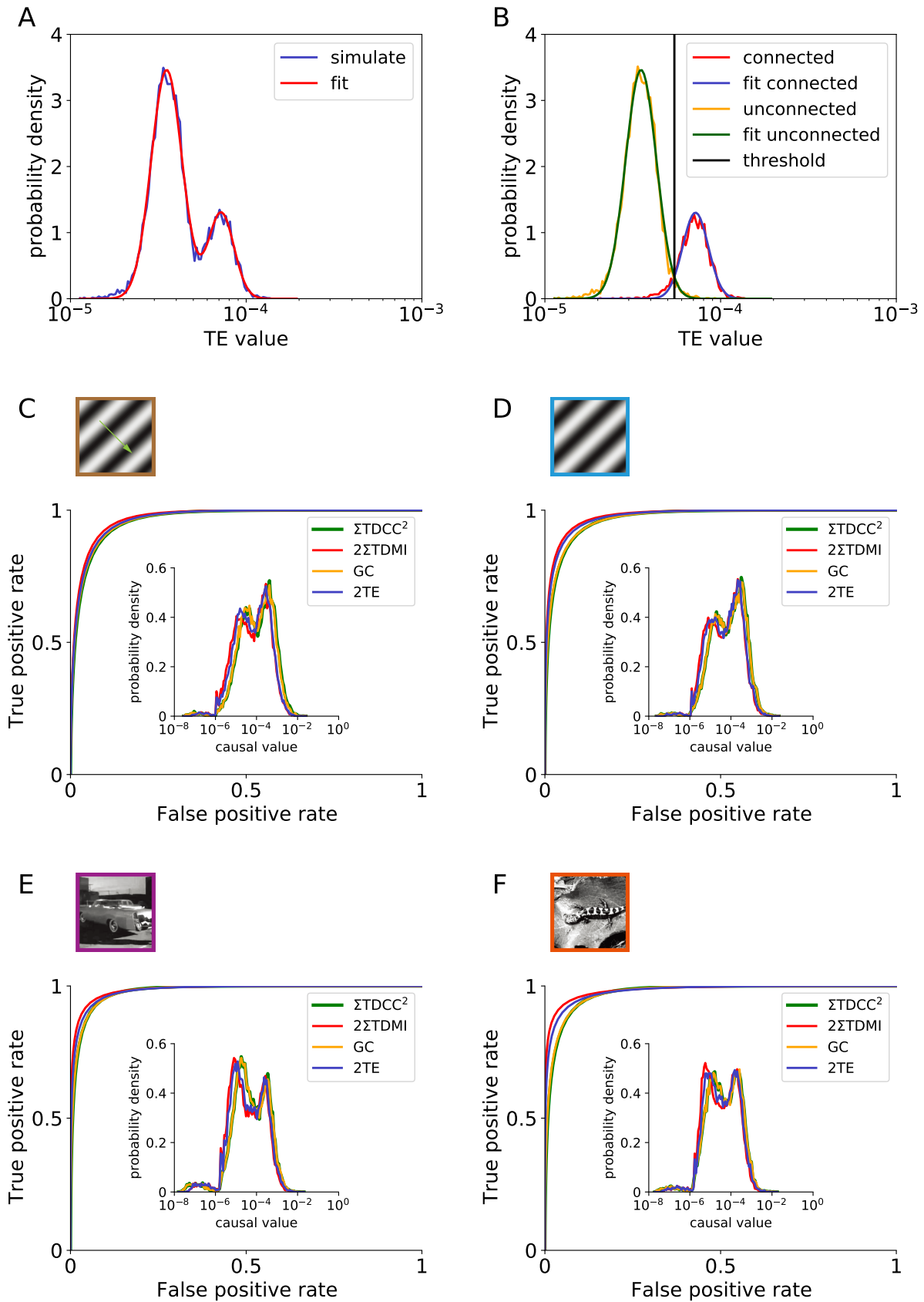


Figure 5: Reconstruction of structural connectivity by the assumption of mixed log-normal distribution of causal values. (A) Distribution of TE values in an HH network of 100 excitatory neurons receiving correlated external Poisson input. The correlation coefficient of the Poisson input to each neuron is 0.3. The blue and red curves are the simulated and fitted distributions, respectively. (B) Distributions of TE values from connected and unconnected pairs of HH neurons in (A). The red and orange curves are the simulated TE values from connected and unconnected pairs respectively while the blue and green curves are the fitted TE values from connected and unconnected pairs respectively which are obtained from the fitting in (A). The parameters are the same as those in Fig. 4. (C-F): ROC curves of the network composed by the recorded neurons in experiment under visual stimuli of (C) drifting gratings, (D) static

connectivity to evaluate the performance of network connectivity reconstruction, *e.g.*, the AUC value is 0.997 in Fig. 5B. In addition, we also provide the optimal inference threshold of TE values as the intersection of the fitted curves [39] indicated by the vertical solid line in Fig. 5B.

We then apply the same ROC analysis to the causality measures from experimental data with different visual stimuli conditions. As shown in the insets of Figs. 5C-F, the distribution of TDCC, TDMI, GC, and TE values are very close, which again verifies their mathematical relations given by Theorems 1-4. Under the assumption of mixed log-normal distribution (*SI Appendix*, Figs. S7A-D), we first infer the ground truth of the network structural connectivity, and then evaluate the reconstruction performance of TDCC, TDMI, GC, and TE by the ROC curves which nearly overlap as shown in Figs. 5C-F with AUC values greater than 0.97. We also infer the binary adjacency matrix using the optimal inference threshold (*Materials and Methods*) from ROC analysis. The reconstructed adjacency matrix from all four different condition of visual stimuli are consistent, in which more than 89% of the total pairs are consistently classified into true positive and true negative population of inferred connections. Almost all of the causal values of inconsistently inferred connections fall into the overlapping region of the connected and unconnected distributions, *i.e.*, the causal values from connected (unconnected) pairs but less (greater) than the threshold (green curve in *SI Appendix*, Figs. S7E-H) which are generally error prone. Comparing the reconstructed structural connectivity of an HH network driven by different correlated Poisson inputs, the inconsistent causal values also mainly fall on the overlapping region (*SI Appendix*, Fig. S8).

Discussion

In this work, we have revealed the quantitative relations among four widely used causality measures (TDCC, TDMI, GC, and TE) for pulse-like signals, and have demonstrated their capability for reconstructing the physical (structure) connectivity using the example of HH neural network. Meanwhile, these causal inference methods also can be successfully applied to reconstruct the connectivity of a subnetwork while the neuronal activities beyond the subnetwork are not observable. Then, we have applied them to reconstruct the structural connectivity of the real neuronal network in mouse brain using spike train data, which have been massively recorded by calcium imaging [4,40,41] or single and multiple electrodes [2,42,43] in experiments, and have achieved promising performances.

To emphasize the essence of effective reconstruction for pulse-like signals in our framework, we again address the fact that i) they have small correlation length, and ii) their indirect causalities are much weaker than direct ones. On the one hand, the auto-correlation function of pulse-like signals rapidly decay with the shrinkage of time step Δt (*SI Appendix* Fig. S1). It protects the inferred causality from the corruption of the self-memory of time series. Also, it allows us to use a small k and l ($k = l = 1$) in application which overcomes the curse of dimensionality in the estimation of probability distribution and provides a practical approach for network reconstruction. On the other hand, the value of indirect causality is as several orders of magnitude smaller than direct one, which ensures the feasibility of distinguishing the directed connections from indirect ones according to their magnitudes of causal connectivity. With those property of pulse-like signals, it is worth pointing out that the application of the simplest statistic, TDCC, is sufficient enough to reconstruct the connectivity of neuronal networks with spike trains as measured signals. In contrast, if these causality measures are directly applied to continuous-valued signals, *e.g.*, voltage time series, the mathematical relations derived in our theorems become invalid (*SI Appendix*, Fig. S9A). Moreover, TDCC and TDMI may give incorrect reconstruction of the structural connectivity due to the strong self-correlation of continuous-valued time series (*SI Appendix*, Fig. S9B).

Although we have illustrated the effectiveness of the four causality measures taking the examples of excitatory HH neural network receiving uncorrelated external Poisson drive (*Materials and Methods*), we find that these measures are applicable to more general situations, including networks in different dynamical states, networks receiving correlated inputs, networks with both excitatory and inhibitory neurons, networks with different neuronal model, and other pulse-output networks beyond neural systems.

First, oscillations and synchronizations are commonly observed in the biological brain network, as shown in *SI Appendix, Fig. S10A*. Due to the fake causality between neurons introduced by the strong synchronous state, conventional reconstruction frameworks fail to capture the true structural connectivity. However, with our framework, high inference accuracy ($AUC > 0.88$) can still be achieved (shown in *SI Appendix, Figs. S10B-C*). Furthermore, by applying a desynchronized sampling method that only samples the pulse-output signals in the asynchronous time interval (*SI Appendix, Fig. S10D*), we can again perfectly reconstruct the network ($AUC > 0.99$), shown in *SI Appendix, Figs. S10E-F*. The relation between percentages of desynchronized downsampling and AUC values is shown in *SI Appendix, Fig. S11*.

Second, external inputs of the network in the brain can be often correlated. In such a case, the synchronized states can be achieved similarly compared with previous cases (shown in *SI Appendix, Fig. S12A*). Similarly, our framework can still achieve high inference accuracy ($AUC > 0.99$ with desynchronized downsampling methods, or $AUC > 0.88$ without downsampling) if the external inputs are moderately correlated (*e.g.*, correlation coefficient less than 0.35 in our simulation case, see *SI Appendix, Figs. S12 B-F*).

Third, for the more general networks containing both excitatory and inhibitory neurons, we show that performance of the reconstruction remains the same for an HH network of both excitatory and inhibitory neurons ($AUC > 0.99$ with desynchronized downsampling methods, or $AUC > 0.71$ without downsampling) (*SI Appendix, Fig. S13*).

Fourth, we also apply our framework of reconstruction onto other types of neuronal networks. Here we take the current-based leaky integrate-and-fire (LIF) neuronal network containing 100 excitatory LIF neurons (*Materials and Methods*) randomly connected with probability 0.25 as an example (*SI Appendix, Fig. S14A*). Our framework still works for LIF network, with well separated two-modal distribution of causality values (*SI Appendix, Fig. S14B*) and high reconstruction performance ($AUC > 0.99$) (*SI Appendix, Fig. S14C*).

Last but not least, we point out that the mathematical relations among four causality measures and their successful application to reconstruct the structural connectivity is general for a wide range of pulse-output nonlinear networks. Here, we apply our framework onto the pulse-output Lorenz networks (*Materials and Methods*) with 100 pulse-coupled Lorenz nodes, which is proposed for atmospheric convection with chaotic property [44]. The raster of pulse-output signals for the Lorenz network is shown in *SI Appendix, Fig. S14D*. Again, a well separated two-modal distribution of causality values (*SI Appendix, Fig. S14E*) and a high reconstruction performance ($AUC > 0.99$) (*SI Appendix, Fig. S14F*) prove the validity of our inference framework.

Materials-and-Methods

Reconstruction performance evaluation

For binary inference of structural connectivity, analysis based on receiver operating characteristic (ROC) curves is adopted to evaluate the reconstruction performance in this work. The following two scenarios are considered.

With known structural connectivity

The conventional procedures for ROC curves analysis can be naturally applied towards data with true labels, *i.e.* structural connectivity in our binary reconstruction case. The area under the ROC curve (AUC) quantifies how well causality measures can distinguish from structurally connected edges from the other. If AUC is close to 1, the distributions of the causality measures between those of connected edges and disconnected ones are well distinguishable, *i.e.*, the performance of binary reconstruction is

good. If the AUC is close to 0.5, the distribution of those two kinds are virtually indistinguishable, meaning the performance of reconstruction is close to random guess.

Without known structural connectivity

The causality measures for synaptically connected and unconnected pairs of neurons can be fitted by the log-normal distribution with different parameters, *i.e.*, $\log_{10} T_{Y \rightarrow X}^{(\text{con})} \sim \mathcal{N}(\mu_1, \sigma_1^2)$ and $\log_{10} T_{Y \rightarrow X}^{(\text{uncon})} \sim \mathcal{N}(\mu_2, \sigma_2^2)$ where the superscripts “con” and “uncon” indicates a directed synaptic connection and no synaptic connection from Y to X , respectively. Thus, the overall distribution is fitted with the summation of two log-normal distributions

$$\frac{p_c}{\sqrt{2\pi\sigma_1^2}} \exp\left(-\frac{(x - \mu_1)^2}{2\sigma_1^2}\right) + \frac{1 - p_c}{\sqrt{2\pi\sigma_2^2}} \exp\left(-\frac{(x - \mu_2)^2}{2\sigma_2^2}\right),$$

where p_c is the proportional coefficient between two Gaussian distributions $\log_{10} T_{Y \rightarrow X}^{(\text{con})}$ and $\log_{10} T_{Y \rightarrow X}^{(\text{uncon})}$. After that, the fitted distribution of two types of connections are regarded as the true labels of structural connectivity. The similar procedures, as previous case, are applied to get ROC curve and AUC value to evaluate the reconstruction performance of causality measures.

The HH model

The dynamics of the i th neuron of an HH network with N neurons is governed by

$$\begin{aligned} C \frac{dV_i}{dt} &= -G_L(V_i - V_L) + I_i^{\text{Na}} + I_i^{\text{K}} + I_i^{\text{input}} \\ I_i^{\text{Na}} &= -G_{\text{Na}} m_i^3 h_i (V_i - V_{\text{Na}}) \\ I_i^{\text{K}} &= -G_{\text{K}} n_i^4 (V_i - V_{\text{K}}) \\ \frac{dz_i}{dt} &= (1 - z_i) \alpha_z(V_i) - z_i \beta_z(V_i), \quad \text{for } z = m, h, n, \end{aligned}$$

where C and V_i are the neuron’s membrane capacitance and membrane potential, respectively; m_i , h_i , and n_i are gating variables; V_{Na} , V_{K} , and V_L are the reversal potentials for the sodium, potassium, and leak currents, respectively; G_{Na} , G_{K} , and G_L are the corresponding maximum conductance; and α_z and β_z are the rate variables. The detailed dynamics of the gating variables m , h , n can be found in Ref. [39] and *SI Appendix, Supplementary Information Text 3*. The input current $I_i^{\text{input}} = -G_i(t)(V_i - V_E)$ where $G_i(t)$ is the input conductance defined as $G_i(t) = f \sum_l H(t - s_{il}) + \sum_j A_{ij} S \sum_l H(t - \tau_{jl})$ and V_E is the reversal potential of excitation. Here, s_{il} is the l th spike time of the external Poisson input with strength f and rate ν , $\mathbf{A} = (A_{ij})$ is the adjacency matrix with $A_{ij} = 1$ indicating a directed connection from neuron j to neuron i and $A_{ij} = 0$ indicating no connection there. S is the coupling strength, and τ_{jl} is the l th spike time of the j th neuron. The spike-induced conductance change $H(t)$ is defined as $H(t) = \frac{\sigma_d \sigma_r}{\sigma_d - \sigma_r} \left[\exp\left(-\frac{t}{\sigma_d}\right) - \exp\left(-\frac{t}{\sigma_r}\right) \right] \Theta(t)$, where σ_d and σ_r are the decay and rise time scale, respectively, and $\Theta(\cdot)$ is the Heaviside function. When the voltage V_j reaches the firing threshold, V_j^{th} , the j th neuron generates a spike at this time, say τ_{jl} , and it will induce the i th neuron’s conductance change if $A_{ij} = 1$.

Current-based LIF model

The dynamics of the i th current-based leaky integrate-and-fire (LIF) neuron is governed by

$$C \frac{dV_i}{dt} = -G_L(V_i - V_L) + I_i^{\text{input}}$$

$$V_i(t) = V_{\text{reset}} \quad \text{if} \quad V_i(t) \geq V^{\text{th}},$$

where C and V_i are the membrane capacitance and membrane potential (voltage). V_L and G_L are the reversal potentials and conductance for leak currents. Compared with HH model, current-based LIF model drops terms of nonlinear sodium and potassium current, and replaces the conductance-based input current with the current-based one, $I_i^{\text{input}} = f \sum_l \delta(t - s_{il}) + \sum_j A_{ij} S \sum_l \delta(t - \tau_{jl})$, where s_{il} is the l th spike time of external Poisson input with strength f and rate ν , and τ_{jl} is the l th spike time of j th neuron with strength S . And $\mathbf{A} = A_{ij}$ is the adjacency matrix defined the same as those in the HH model. When the voltage reaches the threshold V^{th} , the i th neuron will emit a spike to all its connected post-synaptic neurons, and then reset to V_{reset} immediately. In numerical simulation, we use dimensionless quantities: $C = 1$, $V_R = 0$, $V^{\text{th}} = 1$, and the leakage conductance is set to be $G_L = 0.05\text{ms}^{-1}$ corresponding to the membrane time constant of 20ms.

Pulse-output Lorenz network

The dynamics of the i th node of a Lorenz network is governed by

$$\frac{dx_i}{dt} = \sigma(y_i - x_i) + \sum_j A_{ij} S \sum_l \delta(t - \tau_{jl})$$

$$\frac{dy_i}{dt} = \rho x_i - y_i - x_i z_i$$

$$\frac{dz_i}{dt} = -\beta z_i + x_i y_i,$$

where $\sigma = 10$, $\beta = 8/3$, $\rho = 28$. τ_{jl} is the l -th output time of the j -th node determined by the following. When x_j reaches a threshold $x^{\text{th}} = 10$, it generates a pulse that induces a change in x of all of its post nodes.

Neurophysiological data

The public spike train data is from Allen brain observatory [37], accessed via the Allen Software Development Kit (AllenSDK) [45]. Specifically, the data labeled with sessions-ID 715093703 was analyzed in this work. The 118-day-old male mouse passively received multiple visual stimuli from one of four categories, including drift gratings, static gratings, natural scenes and natural movies. The single neuronal activities, i.e. spike trains, were recorded from 13 distinct brain areas, including APN, CA1, CA3, DG, LGd, LP, PO, VISam, VISl, VISp, VISpm, VISrl, and grey, using 6 Neuropixel probes. For each category of stimulus, the recording lasts for more than 40 minutes. 884 sorted spike trains were recorded in this session and 131 of those were used for causality analysis with signal-to-noise ratio greater than 4.

References

- [1] Bratislav Mišić and Olaf Sporns. From regions to connections and networks: New bridges between brain and behavior. *Curr. Opin. Neurobiol.*, 40:1–7, 2016.
- [2] Carsen Stringer, Marius Pachitariu, Nicholas Steinmetz, Charu Bai Reddy, Matteo Carandini, and Kenneth D. Harris. Spontaneous behaviors drive multidimensional, brainwide activity. *Science (80-.)*, 364(6437), 2019.
- [3] Bruce C Wheeler and Yoonkey Nam. In Vitro Microelectrode Array Technology and Neural Recordings. *Crit. Rev. Biomed. Eng.*, 39(1):45–61, 2011.

- [4] Christoph Stosiek, Olga Garaschuk, Knut Holthoff, and Arthur Konnerth. In vivo two-photon calcium imaging of neuronal networks. *Proc. Natl. Acad. Sci. U. S. A.*, 100(12):7319–7324, 2003.
- [5] C. J. Honey, O. Sporns, L. Cammoun, X. Gigandet, J. P. Thiran, R. Meuli, and P. Hagmann. Predicting human resting-state functional connectivity from structural connectivity. *Proc. Natl. Acad. Sci.*, 106(6):2035–2040, feb 2009.
- [6] Christopher J Honey, Jean-Philippe Thivierge, and Olaf Sporns. Can structure predict function in the human brain? *Neuroimage*, 52(3):766–776, 2010.
- [7] Laura E Suárez, Ross D Markello, Richard F Betzel, and Bratislav Misisic. Linking Structure and Function in Macroscale Brain Networks. *Trends Cogn. Sci.*, 24(4):302–315, 2020.
- [8] Jacob Benesty, Jingdong Chen, Yiteng Huang, and Israel Cohen. Pearson correlation coefficient. In *Springer Top. Signal Process.*, volume 2, pages 1–4. Springer, 2009.
- [9] Michael B. Eisen, Paul T. Spellman, Patrick O. Brown, and David Botstein. Cluster analysis and display of genome-wide expression patterns. *Proc. Natl. Acad. Sci. U. S. A.*, 95(25):14863–14868, 1998.
- [10] Shinya Ito, Michael E. Hansen, Randy Heiland, Andrew Lumsdaine, Alan M. Litke, and John M. Beggs. Extending transfer entropy improves identification of effective connectivity in a spiking cortical network model. *PLoS One*, 6(11):e27431, 2011.
- [11] Purvis Bedenbaugh and George L. Gerstein. Multiunit Normalized Cross Correlation Differs from the Average Single-Unit Normalized Correlation. *Neural Comput.*, 9(6):1265–1275, 1997.
- [12] John A. Vastano and Harry L. Swinney. Information transport in spatiotemporal systems. *Phys. Rev. Lett.*, 60(18):1773–1776, 1988.
- [13] Thomas Schreiber. Measuring information transfer. *Phys. Rev. Lett.*, 85(2):461–464, 2000.
- [14] Stefan Frenzel and Bernd Pompe. Partial mutual information for coupling analysis of multivariate time series. *Phys. Rev. Lett.*, 99(20):204101, 2007.
- [15] Patrick W. McLaughlin, Vrinda Narayana, Marc Kessler, Daniel McShan, Sara Troyer, Lon Marsh, George Hixson, and Peter L. Roberson. The use of mutual information in registration of CT and MRI datasets post permanent implant. *Brachytherapy*, 3(2):61–70, 2004.
- [16] C. W. J. Granger. Investigating Causal Relations by Econometric Models and Cross-spectral Methods. *Econometrica*, 37(3):424, 1969.
- [17] Steven L. Bressler and Anil K. Seth. Wiener-Granger Causality: A well established methodology. *Neuroimage*, 58(2):323–329, 2011.
- [18] Lionel Barnett, Adam B. Barrett, and Anil K. Seth. Solved problems for Granger causality in neuroscience: A response to Stokes and Purdon. *Neuroimage*, 178:744–748, 2018.
- [19] Terry Bossomaier, Lionel Barnett, Michael Harré, and Joseph T. Lizier. An introduction to transfer entropy: Information flow in complex systems. *An Introd. to Transf. Entropy Inf. Flow Complex Syst.*, pages 1–190, 2016.
- [20] Javier Borge-Holthoefer, Nicola Perra, Bruno Gonçalves, Sandra González-Bailón, Alex Arenas, Yamir Moreno, and Alessandro Vespignani. The dynamics of information-driven coordination phenomena: A transfer entropy analysis. *Sci. Adv.*, 2(4):e1501158, 2016.
- [21] Songting Li, Yanyang Xiao, Douglas Zhou, and David Cai. Causal inference in nonlinear systems: Granger causality versus time-delayed mutual information. *Phys. Rev. E*, 97(5):52216, 2018.
- [22] Jakob Runge, Jobst Heitzig, Vladimir Petoukhov, and Jürgen Kurths. Escaping the curse of dimensionality in estimating multivariate transfer entropy. *Phys. Rev. Lett.*, 108(25):258701, 2012.
- [23] Evan W. Newell and Yang Cheng. Mass cytometry: Blessed with the curse of dimensionality. *Nat. Immunol.*, 17(8):890–895, 2016.
- [24] Francis Bach. Breaking the curse of dimensionality with convex neural networks. *J. Mach. Learn. Res.*, 18(1):1–53, 2017.

- [25] Daniel Marbach, Robert J. Prill, Thomas Schaffter, Claudio Mattiussi, Dario Floreano, and Gustavo Stolovitzky. Revealing strengths and weaknesses of methods for gene network inference. *Proc. Natl. Acad. Sci. U. S. A.*, 107(14):6286–6291, 2010.
- [26] Riet De Smet and Kathleen Marchal. Advantages and limitations of current network inference methods. *Nat. Rev. Microbiol.*, 8(10):717–729, 2010.
- [27] Cunlu Zou, Katherine J. Denby, and Jianfeng Feng. Granger causality vs. dynamic Bayesian network inference: A comparative study. *BMC Bioinformatics*, 10(1):122, 2009.
- [28] Lionel Barnett, Adam B. Barrett, and Anil K. Seth. Granger causality and transfer entropy Are equivalent for gaussian variables. *Phys. Rev. Lett.*, 103(23):238701, 2009.
- [29] Martin A. Koch, David G. Norris, and Margret Hund-Georgiadis. An investigation of functional and anatomical connectivity using magnetic resonance imaging. *Neuroimage*, 16(1):241–250, 2002.
- [30] Anil Seth. Causal connectivity of evolved neural networks during behavior. *Netw. Comput. Neural Syst.*, 16(1):35–54, 2005.
- [31] Felix Schiele, Joanne Van Ryn, Keith Canada, Corey Newsome, Eliud Sepulveda, John Park, Herbert Nar, and Tobias Litzenburger. A specific antidote for dabigatran: Functional and structural characterization. *Blood*, 121(18):3554–3562, 2013.
- [32] Shuixia Guo, Jianhua Wu, Mingzhou Ding, and Jianfeng Feng. Uncovering interactions in the frequency domain. *PLoS Comput. Biol.*, 4(5):e1000087, 2008.
- [33] Boris Gourévitch and Jos J. Eggermont. Evaluating information transfer between auditory cortical neurons. *J. Neurophysiol.*, 97(3):2533–2543, 2007.
- [34] Raul Vicente, Michael Wibral, Michael Lindner, and Gordon Pipa. Transfer entropy—a model-free measure of effective connectivity for the neurosciences. *J. Comput. Neurosci.*, 30(1):45–67, 2011.
- [35] Tom Fawcett. An introduction to ROC analysis. *Pattern Recognit. Lett.*, 27(8):861–874, 2006.
- [36] Jane V. Carter, Jianmin Pan, Shesh N. Rai, and Susan Galandiuk. ROC-ing along: Evaluation and interpretation of receiver operating characteristic curves. *Surg. (United States)*, 159(6):1638–1645, 2016.
- [37] Allen Institute for Brain Science. Allen Brain Observatory, 2016.
- [38] György Buzsáki and Kenji Mizuseki. The log-dynamic brain: How skewed distributions affect network operations. *Nat. Rev. Neurosci.*, 15(4):264–278, 2014.
- [39] Wesley J. Wildman, Richard Sosis, and Patrick McNamara. *Theoretical Neuroscience*, volume 4. Cambridge, MA: MIT Press, 2014.
- [40] Benjamin F. Grewe, Dominik Langer, Hansjörg Kasper, Björn M. Kampa, and Fritjof Helmchen. Erratum: High-speed in vivo calcium imaging reveals neuronal network activity with near-millisecond precision (Nature Methods (2010) 7 (399-405)). *Nat. Methods*, 7(6):479, 2010.
- [41] Hod Dana, Yi Sun, Boaz Mohar, Brad K. Hulse, Aaron M. Kerlin, Jeremy P. Hasseman, Getahun Tsegaye, Arthur Tsang, Allan Wong, Ronak Patel, John J. Macklin, Yang Chen, Arthur Konnerth, Vivek Jayaraman, Loren L. Looger, Eric R. Schreier, Karel Svoboda, and Douglas S. Kim. High-performance calcium sensors for imaging activity in neuronal populations and microcompartments. *Nat. Methods*, 16(7):649–657, 2019.
- [42] Greg D. Field, Jeffrey L. Gauthier, Alexander Sher, Martin Greschner, Timothy A. MacHado, Lauren H. Jepson, Jonathon Shlens, Deborah E. Gunning, Keith Mathieson, Wladyslaw Dabrowski, Liam Paninski, Alan M. Litke, and E. J. Chichilnisky. Functional connectivity in the retina at the resolution of photoreceptors. *Nature*, 467(7316):673–677, 2010.
- [43] James J. Jun, Nicholas A. Steinmetz, Joshua H. Siegle, Daniel J. Denman, Marius Bauza, Brian Barbarits, Albert K. Lee, Costas A. Anastassiou, Alexandru Andrei, Çağatay Aydin, Mladen Barbic, Timothy J. Blanche, Vincent Bonin, João Couto, Barundeb Dutta, Sergey L. Gratiy, Diego A. Gutnisky, Michael Häusser, Bill Karsh, Peter Ledochowitsch, Carolina Mora Lopez, Catalin Mitelut, Silke Musa, Michael Okun, Marius Pachitariu, Jan Putzeys, P. Dylan Rich, Cyrille Rossant, Wei Lung Sun, Karel Svoboda, Matteo Carandini, Kenneth D. Harris, Christof Koch, John O’Keefe, and Timothy D. Harris. Fully integrated silicon probes for high-density recording of neural activity. *Nature*, 551(7679):232–236, 2017.

- [44] Edward N. Lorenz. Deterministic nonperiodic flow. *Universality Chaos, Second Ed.*, 20(2):367–378, 2017.
- [45] Allen Institute for Brain Science. Allen SDK Documentation, 2018.